

**Interlayer Bonding Strength of 3D Printed PEEK Specimens**

Journal:	<i>Soft Matter</i>
Manuscript ID	SM-ART-03-2021-000417
Article Type:	Paper
Date Submitted by the Author:	17-Mar-2021
Complete List of Authors:	Liaw, Chya-Yan; New Jersey Institute of Technology Newark College of Engineering, Chemical and Materials Engineering Tolbert, John; Lehigh University, Materials Science and Engineering Chow, Lesley; Lehigh University, Materials Science and Engineering; Lehigh University, Guvendiren, Murat; New Jersey Institute of Technology Newark College of Engineering,

ARTICLE

Interlayer Bonding Strength of 3D Printed PEEK Specimens

Chya-Yan Liaw^a, John W. Tolbert^c, Lesley W. Chow^{cd} and Murat Guvendiren^{*ab}aReceived 00th January 20xx,
Accepted 00th January 20xx

DOI: 10.1039/x0xx00000x

Recent advances in extrusion-based filament 3D printing technology enable the processability of high-performance polymers. Poly(ether ether ketone) (PEEK) is an important group of high-performance polymer that has been widely used in aerospace, automotive, and biomedical applications. The interlayer bonding strength of 3D printed PEEK is crucial for load-bearing applications, yet studies on 3D printed PEEK are sparse due to processing challenges. In this study, the three-point flexural test is used to study the interlayer bonding strength of 3D-printed PEEK specimens with respect to the printing process parameters, including nozzle temperature, print speed, layer height, and wait-time. A design of experiment (DOE) approach is developed to study correlations between printing parameters and the end-use properties, including flexural stress (σ_f) and strain at break (ε_f), flexural modulus (E_f), and crystallinity (χ). Our results show that the nozzle temperature, layer height, and wait-time significantly affect the interlayer bonding strength, with nozzle temperature being the most influential parameter to enhance interlayer bonding strength indicated by a significant increase in σ_f , ε_f , and χ . Thermal annealing post-printing is shown to increase the degree of χ and E_f , yet its effect on interlayer bonding strength is minimal, indicating that the interlayer bonding strength is primarily determined during the printing process. This study demonstrates the use of a three-point flexural test integrated with a versatile and robust DOE approach to study the interlayer bonding strength of PEEK to reduce product development time while improving mechanical properties.

Introduction

Additive manufacturing (AM) has become a commonly used advanced manufacturing method to fabricate prototypes, parts, and fully functional devices. Compared to conventional manufacturing approaches, it offers several advantages including custom-design, high-complexity, on-demand fabrication, and low-cost. Extrusion-based 3D printing from polymer filaments, usually referred to as fused filament fabrication (FFF), also known under the trademark name fused deposition modeling (FDM), is the most commonly used AM technique due to its availability, low-cost and ease of operation. FFF process involves extrusion and deposition of a melted thermoplastic filament in the form of a strut onto a build platform, where it cools and solidifies to form a solid strut. This

process follows a layer-by-layer deposition process to form a 3D object. Although extrusion-based filament printing has been widely used in various industries, this technology has not yet been adopted into the mainstream of production or replace the conventional manufacturing processes (such as injection molding) for mass production of robust products. One of the notable barriers to the implementation of 3D printing is the limited and anisotropic mechanical properties of the printed parts^{1,2}, i.e., the mechanical strength across layers (in the build-direction or z-direction) is usually weaker than the mechanical strength in the x- and y-direction (or xy-plane). The reasons for the anisotropic nature can be listed as (i) formation of gaps and voids at the interface, (ii) development of a weak interlayer bonding due to limited welding, and (iii) generation of high residual stresses along with the interface due to repeated thermal expansion and contraction during the printing process. The anisotropic nature of 3D printed parts often leads to layer delamination, which usually occurs suddenly, leading to brittle fracture.^{3,4} This phenomenon is found to be more pronounced in extrusion-based filament printing with a reduction in strength in the range of ~35%-90% when compared to other 3D printing techniques, such as selective laser sintering (SLS) with ~10% reduction and stereolithography (SLA) with ~1% reduction.⁵⁻⁷ Moreover, while the strength reduction in build direction occurs in all FFF-fabricated polymers, it is more prominent for semicrystalline polymers, making it more challenging to process than amorphous polymers. Therefore, it is critical to develop a robust testing approach to study the effect of processing parameters on the interlayer mechanical properties of the 3D printed parts to prevent part failure, which could potentially broaden their practical applications.

^a Otto H. York Department of Chemical and Materials Engineering, New Jersey Institute of Technology, Newark, NJ, 07102, USA..

^b Department of Biomedical Engineering, New Jersey Institute of Technology, Newark, NJ, 07102, USA.

^c Department of Materials Science and Engineering, Lehigh University, Bethlehem, PA 18015, USA

^d Department of Bioengineering, Lehigh University, Bethlehem, PA 18015, USA

† Footnotes relating to the title and/or authors should appear here.

Electronic Supplementary Information (ESI) available: [Figure S1. SEM images of the fractured surfaces; Figure S2. DSC curves for the 3D-printed PEEK samples; Figure S3. Leverage residual plots of the significant factors for each response; Figure S4. Bar plots of stress at break versus strain at break, stress at break versus modulus, and stress at break versus crystallinity; Figure S5. Scattered plots showing the correlation between strain at break and crystallinity, strain at break and modulus, modulus and crystallinity; Table S1. Experimental design matrix. Table S2. Parameters and coefficients for DOE models. Table S3. Shift factors and zero-shear viscosity values. Regression Model Evaluation section.].

See DOI: 10.1039/x0xx00000x

In recent years, there has been a growing interest in 3D printing of high-performance polymers such as poly(ether ether ketone) (PEEK), poly(etherimide) (PEI), poly(phenylsulfone) (PSU), and poly(ether ketone ketone) (PEKK).^{8, 9} PEEK is an engineering thermoplastic and exhibits excellent chemical resistance, mechanical performance, and dimensional stability under high-temperature (up to 260°C) and high-pressure environments.³ Therefore, PEEK has been commonly used in applications subjected to severe conditions such as aerospace, automotive, oil and gas applications, and semiconductor manufacturing processes. Additionally, PEEK has become an important group of biomaterials for medical applications and a strong candidate as an alternative to replace metal and ceramic implants.¹⁰ PEEK is resistant to hydrolysis (in hot water and under gamma, beta, and X-rays), thus it is amenable to sterilization. It is biocompatible and lightweight, and has an elastic modulus similar to that of cortical bone.¹¹ PEEK products have been made by SLS technology for quite a long time, while commercially formulating PEEK into filaments for extrusion-based printing is relatively new.^{10, 12} Valentin and co-workers were the first to show the feasibility of PEEK printing using a specially developed filament printer.¹³ It is challenging to fabricate extrusion-based printed PEEK parts due to several reasons.⁹ First, it requires high print temperatures (360°C - 450°C) and is resistant to common solvents. Second, PEEK is more sensitive to variations in thermal processing conditions with respect to amorphous filaments (such as ABS, HIPS (High Impact Polystyrene), and PEI) due to its semi-crystalline nature. Finally, PEEK exhibits relatively rapid crystallization kinetics and substantial dimensional shrinkage upon cooling. The thermal expansion and shrinkage are constrained by fused layers, which results in the generation of high residual stresses within the printed parts. Precise control of the thermal processing conditions could reduce residual stress and improve print quality. In addition, the crystallinity reduces the ability of chain diffusion and entanglement during the printing process, leading to a decrease in the interlayer bonding strength. The high residual stress and weak interlayer bonding can potentially lead to the formation of cracks between layers under stress.

There are relatively few studies focusing on extrusion-based printing of PEEK due to the difficulties mentioned above. The majority of these studies focus on the role of thermal processing parameters (nozzle, platform and ambient temperature, and post-printing heat treatment methods)¹⁴⁻¹⁸ or non-thermal processing parameters (strut/build orientation, layer height, infill density, print speed, and reinforcement content, such as concentration of carbon nanotubes)^{3, 12, 19-28} on the mechanical properties and microstructure of the 3D printed parts. For example, Vaezi and Yang showed that nozzle temperature and ambient temperature are important factors to prevent PEEK/substrate detachment and layer delamination.¹⁷ Yang et al. investigated the relationship between various thermal conditions and crystallinity as well as mechanical properties.¹⁴ Their results showed that the degree of crystallinity and tensile properties are greatly affected by the ambient and the nozzle

temperature. Arif et al. conducted tensile, flexural, and fracture tests on PEEK, which were printed horizontally with raster angles of 0° (H0) and 90° (H90), and vertically with a raster angle of 90° (V90).¹⁹ They reported that H0 showed the highest mechanical performance, followed by H90 and V90. Magri et al. carried out tensile testing on horizontally-printed PEEK dogbone samples.²⁴ They suggested an optimal tensile strength can be achieved for annealed parts postprinting that were printed at 400°C, at 30 mm/s, for 0.15 mm layer thickness and a raster angle of 0°/15°/-15°. Here, we would like to note that the majority of these studies focused on either testing the mechanical properties of the horizontally-printed specimens or comparing the mechanical properties between horizontally and vertically printed specimens. When horizontally-printed specimens are used, the stress is mainly carried out by the printed strands, not by the interface between layers. Thus, there is a critical need to determine the influence of process parameters on the interlayer bonding strength of the 3D printed PEEK.

A summary of the state-of-the-art to determine the interlayer bonding strength of FFF-printed PEEK specimens is given in **Table 1**. For each study, Table 1 summarizes the test type, sample geometry, studied factors, controlled conditions, and major findings. Several test methods were reported including tensile tests using dogbones,^{19, 29} flexural tests using coupons,^{19, 22, 23, 30-32} and compression tests using lumbar spinal cages³³. The majority of these test samples were fabricated by machining from a single-wall/multiple-wall hollow rectangular box^{29, 32, 34} or cut from an annular rectangular part.^{23, 30} Note that the stresses during cutting could potentially induce defects, cracks, or even breakage in the specimens, and the heat generated during milling could lead to localized melting, altering the as-printed specimen properties.³² Additionally, other commonly utilized mode III tear^{35, 36} or single-wall tensile tests^{29, 34} target a single interface and lack the influence from neighboring filaments, resulting in data that may not translate to thick and large-scale components with multiple toolpaths. Several studies have used flexural tests to study PEEK interlayer bonding strength, where tensile properties were examined on flat samples printed horizontally. During these test, the applied stress was parallel to the layers, and the failure was due to shear delamination.^{37, 38}

In this work, we investigated the interlayer bonding strength of the 3D printed PEEK specimens using a three-point flexural test. During the flexural test, the tensile force at the lower surface was loaded along the weakest direction, i.e., the interface between print layers. Therefore the failure mode was governed by the resistance between the layers. Our approach not only eliminated the need for post-processing steps but also ensured interlayer fracture. Note that flexural tests were also reported in the literature to examine the interlayer bond strength of 3D-printed materials.^{6, 19, 39, 40} Here, we presented a DOE (Design of Experiment) approach, in which a fractional factorial screening design was used to plan, analyze, and interpret the results of PEEK interlayer bonding strength. In particular, we investigated

Table 1. Reported literature on interlayer bonding evaluation of FFF-printed PEEK.

Test Type	Sample Geometry	Studied Factors	Controlled Conditions	Major Findings
Compression, compression shear, torsion	Lumber spinal cages	Print speed (1500mm/min, 2000mm/min) Annealing temperature (200°C, 300°C)	Nozzle Temp: 390-410°C Layer height: 0.1 mm Bed temp: 100°C Chamber temp: NA	Annealing didn't result in significant improvement in mechanical properties or decrease in porosity at either annealing temperature.[Ref 33]
Flexural test with load parallel to interlayers	Cut rectangular plaque from an annular rectangular part	Applied laser power (0-10W)	Nozzle temp: 410°C Layer height: 0.2 mm Bed temp: NA Chamber temp: NA Print speed: 6 mm/s	Interlayer shear strength and crystallinity were improved by 45% and 34.5%, respectively.[Ref 30]
Tensile test	Cut tensile bar from a single-wall box	Applied laser power (0-2.75W)	Nozzle temp: 380°C Layer height: 0.2 mm Bed temp: 150°C Chamber temp: 80°C Print speed: 10 mm/s Extrusion width: 1mm	Tensile strength of laser-treated samples was improved by 350% compared to no-treated samples, and 99.5% isotropy was achieved.[Ref 29]
Flexural test with load parallel to interlayers	Cut rectangular plaque from an annular rectangular part	PEEK grade (150G, 450G) Impregnation method between carbon fiber tow and PEEK Laser power	Nozzle temp: 380°C Layer height: 0.2-0.3 mm Bed temp: NA Chamber temp: NA Print speed: NA	Overcame interlayer delamination problems of carbon fiber tow/PEEK composites by adjusting the viscosity of PEEK matrix, implementing pre-impregnation, and applying laser in-situ heating.[Ref 23]
Flexural test with load parallel to interlayers	Horizontally-printed tensile bar and flexural test coupon	Carbon nanotube (CNT) loading in PEEK (1%, 5%)	Nozzle temp: 365°C Layer height: 0.2 mm Bed temp: NA Chamber temp: NA Print speed: 30 mm/s	Flexural shear strength decreased with increasing CNT content.[Ref 31]
As shown in studied factors	As shown in studied factors	Sample geometry (tensile, flexural, compact tension) Print direction with respect to loading direction (horizontal-0°, horizontal-90°, vertical-90°)	Nozzle temp: 410°C Layer height: 0.1 mm Bed temp: 100°C Chamber temp: NA Print speed: 800 mm/min Extrusion width: 0.48mm Infill density: 100%	Vertical-90° specimens showed lower tensile, flexural and fracture toughness than the horizontal-0° and horizontal-90° samples.[Ref 19]
Flexural test with load parallel to interlayers	As shown in studied factors	Sample printing orientation (horizontal-0°, horizontal-90°) Neat PEEK and carbon-fiber incorporated PEEK	Nozzle temp: 400°C Layer height: 0.1 mm Bed temp: 160°C Chamber temp: 90°C Print speed: 15 mm/s Raster angle: -45°/45° Nozzle size: 0.4 mm	The addition of carbon fibers increased the crystallinity of the 3D printed parts, decreased the layer-to-layer bonding strength, and changed the fracture mode. Horizontal-90° samples showed higher strengths than that of the Horizontal-0° samples.[Ref 22]
Flexural test with load perpendicular to interlayers	Cut rectangular plaque from the multi-walled box	PEEK grade with different crystallization rate Print scale	Nozzle temp: 450°C, 405°C Layer height: 0.4mm, 2mm Bed temp: 150°C, 105°C Print speed: 40mm/s, 33mm/s Extrusion width: 1mm, 8mm Layer time: 10s, 60s	Higher interlayer bonding strength was achieved using polymers with slow crystallization rate and smaller-scale printing with reduced layer completion time.[Ref 32]

the effect of several processing parameters, including nozzle temperature, layer thickness, print speed, and wait-time, on the flexural modulus, flexural stress and strain at break, and crystallinity, to determine the most critical processing

parameter or parameters influencing the flexural properties and crystallinity.

Results and Discussion

Experimental design

A screening design is developed using DOE to identify the key processing parameters (**Table 2**), including nozzle temperature (T), print speed (PS), layer height (LH), and wait-time (WT), for extrusion-based filament printing of PEEK test samples. The low- and high-values for each processing parameter were determined based on the recommended printing settings (by the PEEK filament supplier) and the preliminary tests performed in our laboratory, and fed into JMP's DOE platform.

Table 2. Investigated process parameters (factors) and their levels.

Process Parameters (Factor)	Abbreviation	Levels		
		Low (-)	Center (0)	High (+)
Nozzle Temp. (°C)	T	370	390	410
Print Speed (mm/s)	PS	20	40	60
Layer Height (mm)	LH	0.1	0.2	0.3
Wait-time (s)	WT	11	18	25

The levels, or settings, of each factor is coded as (+), (-) or (0). In this notation, (+) represents the high setting, (-) represents the low setting, and (0) represents the value that is set halfway between the low and high settings.

Table 3. Experimental design matrix developed by JMP's DOE platform and the corresponding results (responses).

Run ^a	Pattern ^b	Process Parameters (Factors)			
		T (°C)	PS (mm/s)	LH (mm)	WT (s)
1	0000	390	40	0.2	18
2	---+	370	60	0.3	11
3	++--	410	20	0.3	11
4	++++	410	20	0.1	25
5	0000	390	40	0.2	18
6	---+	370	60	0.1	25
7	----	370	20	0.1	11
8	0000	390	40	0.2	18
9	++--	410	60	0.1	11
10	---+	370	20	0.3	25
11	++++	410	60	0.3	25
12	0000	390	40	0.2	18

^a Each Run is a combination of multiple factor settings. ^b Pattern shows the combination of factor settings using the coded values.

The experimental design matrix developed by JMP's DOE platform is given in **Table 3**. The design matrix includes a total of 12 Runs, or sample sets, with distinct combinations of the four processing parameters, each corresponding to a low (-), center (0), and/or high (+) value. For instance, Runs 1, 5, 8, and 12 correspond to the center-values of all parameters, denoted as (0000), with T = 390 °C, PS = 40 mm/s, LH = 0.2 mm, and WT = 18 s. Run 11 corresponds to the sample set with processing parameters equal to the high-values and is denoted as (++++), where T = 410°C, PS = 60 mm/s, LH = 0.3 mm, and WT = 25 s. Run 7 refers to the condition of low-values and is denoted as (----), with T = 370°C, PS = 20 mm/s, LH = 0.1 mm, and WT = 11 s.

The DOE approach developed in this study enabled accurate analysis using fewer samples and the ability to vary multiple parameters simultaneously. Therefore, our DOE approach is more efficient in terms of sample size, time, labor, and cost to evaluate the effects of multiple variables,^{24, 34} as compared to the one-factor-at-a-time (OFAT) approach, which was employed by the majority of the studies in the literature.^{12, 14, 15}

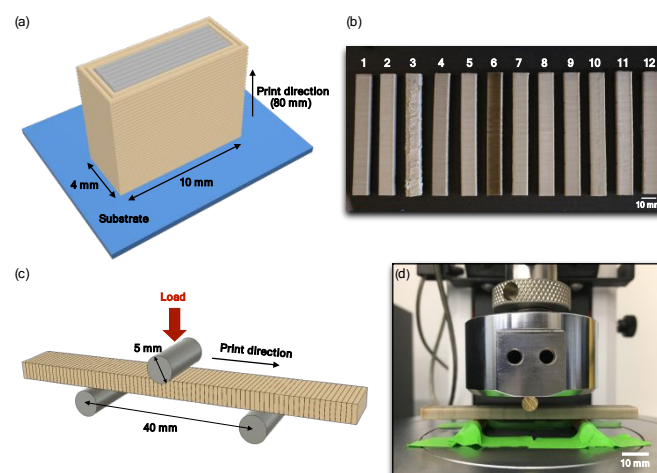


Figure 1. Schematics and images showing the sample preparation and experimental setup. (a) Schematic showing the raster and build orientation of specimens (with dimension in millimeters) for flexural test fabricated. The specimen has two shell layers (beige) and 100% infill (gray). (b) Pictures of the FFF-printed PEEK specimens for each Run or sample group. (c) Schematic of the flexural test setup showing the layer orientation relative to the load direction. (d) Picture of the flexural test setup.

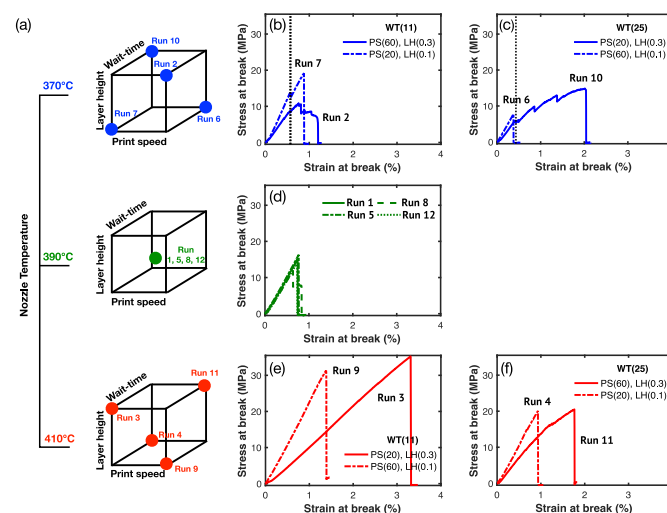


Figure 2. (a) Cube plots showing the experimental design matrix representing the combinations of the process parameters (print speed, layer height and wait-time for each nozzle temperature), which define each Run (i.e., sample set). (b-f) Representative stress-strain plots corresponding to different Runs, where WT, PS and LH denote wait-time, print speed and layer height, respectively.

Mechanical behaviour of the 3D printed test samples

A three-point flexural test was used to investigate the interlayer strength of the 3D printed PEEK (**Figure 1**). The sample sets (i.e., the 12 Runs) were printed using an extrusion-based filament

printer and commercially available PEEK filaments. Digital designs were created using ISO 178 standard, and samples were printed in the vertical direction (Figure 1a). The representative picture of the test samples for each *Run* is given in Figure 1b. During the flexural test, the load is applied perpendicular to the print direction, and to the interface between the print layers (Figure 1c and 1d). Thus, the tensile force generated at the lower surface acts along the interface between print layers, and the failure is governed by the resistance between the layers. The use of flexural tests allowed us for overcoming the inherent difficulty of printing tensile test specimens for PEEK material, including difficulties in achieving required standard sample shape and dimensions, potentially inaccurate and muddled features at the middle section of the dogbone shaped specimens caused by high printing temperatures, small sample cross-section, and short layer time.¹⁹

Figure 2 shows the experimental design matrix using a cube plot for each nozzle temperature (Figure 2a) and the representative stress-strain curves corresponding to different *Runs* (Figure 2b-2f). In Figure 2a, the eight *Runs* from the experimental design are shown at the corners of the cubes, and the four center points are shown at the center of the cube. Several differences in the flexural behavior between sample sets (*Runs*) were observed. For specimens printed at low nozzle temperature ($T = 370^{\circ}\text{C}$), shown in Figure 2b and 2c, the flexural stress showed a linear growth with the strain (corresponding to the elastic region) at low strains ($\sim 0.35\% - 0.55\%$) until the first failure point (sharp decrease in stress) appeared. For *Runs* 2, 7, and 10, after the first failure point, the stress either continued to rise followed by more failure points, or showed multiple significant drops prior to the end of the test. In contrast, *Run* 6 did not show any failure points and exhibited an instant brittle rupture at low strains ($\sim 0.4\%$). The slope of the elastic region is determined by the layer height (LH), such that the smaller the LH, the steeper the slope, and thus, the greater the modulus. Since these test groups (*Runs* 2, 7, and 10) showed several failure points before the catastrophic break, the stress and strain at break were determined at the point where a 5% reduction in stress was observed (shown by the dashed lines in Figures 2b and 2c). In addition, the stress at break was higher when the wait-time was shorter by comparing the overall means for wait-times. For example, the overall mean for wait-time at the level of 11s can be calculated by averaging over the levels of print speed and layer height, which is $(7.8+13.2)/2 = 10.5$ MPa; whereas at the wait-time of 25s, the overall mean of the stress at break is $(7.6+5)/2 = 6.3$ MPa, which is smaller by 4.2 MPa ($10.5 - 6.3$ MPa). For specimens prepared under medium settings (Figure 2d), the stress-strain curves showed brittle failure and were coincident, indicating good repeatability. The stress at break and strain at break were higher ($\sim 0.7\%$) as compared to that of samples printed at $T = 370^{\circ}\text{C}$. For specimens printed at the highest nozzle temperature (Figures 2e and 2f), much larger strains ($\sim 1\% - 3.7\%$) were observed within the elastic range, and the stress at break values were much higher. The fracture mode was predominantly brittle, and no sudden drop in the stress was observed before

the final failure. However, *Run* 11 showed a more ductile behavior where a nonlinear stress-strain relationship was observed. Moreover, the overall mean of the stress at break for wait-time equal to 11s and 25s are $(36.4 + 29.9)/2 = 33.5$ MPa and $(18.2+20.2)/2 = 19.2$ MPa, respectively. The difference between the two overall means ($33.5 - 19.2 = 14.3$ MPa) is much larger than the results obtained at low nozzle temperatures, suggesting that increasing the wait-time could greatly decrease the stress at break when the nozzle temperature is at the highest setting.

The flexural test results for each sample set (*Run*) are summarized in **Table S1 (ESI)**. When evaluating the flexural stress at break and strain at break, the samples from *Run* 3 ($T = 410^{\circ}\text{C}$, PS = 20 mm/s, LH = 0.3 mm, WT = 11s) had the highest values, followed by *Run* 9 ($T = 410^{\circ}\text{C}$, PS = 60 mm/s, LH = 0.1 mm, WT = 11s). *Run* 11 ($T = 410^{\circ}\text{C}$, PS = 60 mm/s, LH = 0.3 mm, WT = 25s) showed slightly better performance than *Run* 4 ($T = 410^{\circ}\text{C}$, PS = 20 mm/s, LH = 0.1 mm, WT = 25s). The nozzle temperature appeared to affect the stress at break and strain at break greatly as all those best-performing samples were printed at the highest temperatures, and their stress at break was in the range of approximately 20 – 35 MPa and strain at break in the range of approximately 1 – 3.5%. Notice that the samples with higher stress at break and strain at break did not necessarily have a higher modulus, which can be seen by comparing *Run* 3 and *Run* 9, and *Run* 11 and *Run* 4. Samples from *Run* 2, 6, 7 and 10, which were printed at the lowest nozzle temperature, showed much weaker mechanical properties with similar values of stress at break (around 8 MPa) and strain at break (around 0.5%). Although the weaker samples had around 70% weaker stress at break and a 75% lower strain at break than the best performing samples, the modulus did not follow the same trend, where some weaker samples (*Run* 6 and *Run* 7) have a higher modulus than the stronger samples (*Run* 3 and *Run* 11).

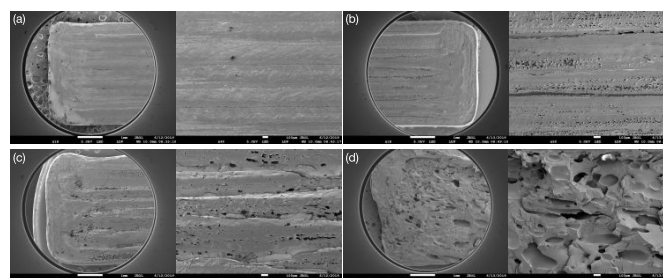


Figure 3. Representative SEM images showing the cross-section of the fracture surfaces for (a) *Run* 6, (b) *Run* 1, (c) *Run* 11, and (d) *Run* 3. For each run, the left image shows the low-magnification view and the right image shows the zoom-in view.

The SEM images of the fracture surfaces of the selected specimens after flexural tests are given in **Figure 3** (see **Figure S1 (ESI)** for a full set of SEM images). The PEEK specimens printed at low nozzle temperature (*Run* 2, 6, 7, and 10) displayed clear welding boundaries between infill strands or between infill strands and the perimeter. It can also be seen that the adjacent filaments within *Run* 6 sample barely touched with each other and had little overlap. These are indications for poor fusion between adjacent struts. The failure surfaces of

these samples were relatively smooth and clean, and almost no pores were observed on the surfaces, indicating that the interlayer bonding strength was weak and the interface broke abruptly. For specimens printed at medium and higher temperatures, the strands seemed to overlap with each other more, and fewer welding boundaries between strands were found owing to sufficient melting of PEEK and improved fluidity at higher printing temperatures, which led to a stronger bonding between infilled strands. Another notable feature of the fractured surface found in the samples printed at medium and high temperatures is the presence of cavities. The average size of the cavities was approximately 15 – 40 μm for samples printed at medium setting (*Run 1, 5, 8, 12*), 30 – 100 μm for samples printed at the highest setting (*Run 9, 11*), and 150 – 250 μm in *Run 3*. The size of cavities correlated with the amount of material within the layer that was being pulled off during fracture and with the force required to pull on the material during delamination. Thus, the increase in cavity size is an indication of greater bonding strength between layers, as can be seen in the stress-strain curves (Figure 2) where *Run 3* showed much higher stress and strain at break, followed by *Run 9, 11*, and then the four center point measurements (*Run 1, 5, 8, 12*).

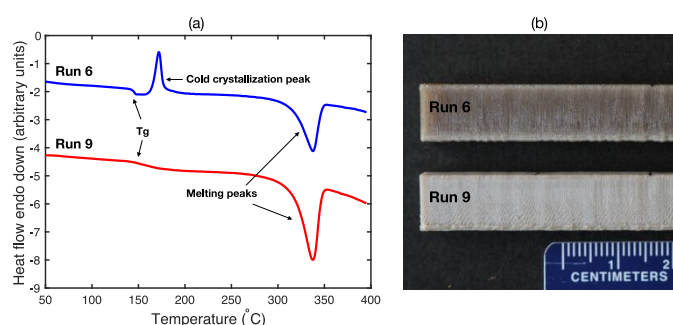


Figure 4. (a) Comparison of DSC 1st heating curves for FFF-printed PEEK samples for *Run 6* (lowest crystallinity group) and *Run 9* (one of the highest crystallinity group). (b) Representative pictures of the samples showing color differences between the two *Runs*.

Thermal behaviour of the 3D printed test samples

To assess the influence of the 3D printing process on the crystallinity of PEEK, the first heating cycle was studied using DSC. Among the 12 *Runs*, the highest degree of crystallinity occurred in *Run 3* (34%), and the lowest crystallinity value of 17.6% occurred in *Run 6* (Table S1, ESI). The samples for the rest of the *Runs* showed crystallinity in the range of 25% – 29%. The results showed a general trend such that an increase in crystallinity corresponds to a higher mechanical strength. When evaluating the mechanical properties for *Runs* excluding *Run 3* and *Run 6*, the mechanical properties are quite different despite smaller variations in crystallinity. Figure 4 shows the representative heating curves for the test samples corresponding to *Run 6* ($T = 370^\circ\text{C}$, PS = 60 mm/s, LH = 0.1 mm, WT = 25s) and *Run 9* ($T = 410^\circ\text{C}$, PS = 60 mm/s, LH = 0.1 mm, WT = 11s). DSC heating profile for *Run 9* is representative of the rest of the *Runs* (Figure S2, ESI), with a glass transition (T_g) at 145°C and a melting peak (T_m) at around 338°C, except for *Run 6*. *Run 6* showed an exothermic cold crystallization peak

at around 168°C, indicating that the as-printed samples underwent incomplete crystallization due to rapid cooling. The cold crystallization is typically induced by heating above the T_g where the amorphous polymer chains gain sufficient mobility to reorganize and align with each other. In good agreement with this behavior, *Run 6* samples appeared brownish compared to *Run 9*, which showed a beige color (Figure 4b). The brownish color indicates the amorphous structure, whereas the beige color is a result of the semi-crystalline structure.²⁵ The amorphous structure in *Run 6* is probably caused by rapid cooling during the printing process or insufficient melting of the polymers when using a low nozzle temperature, or a combination of the two.

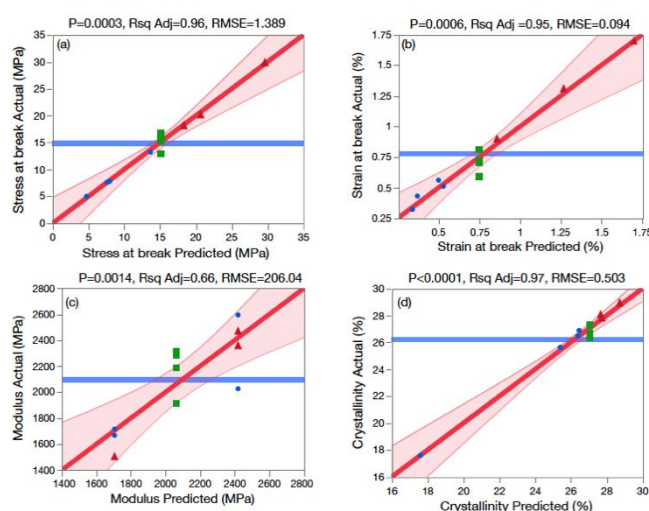


Figure 5. Actual by predicted plots (measured values with respect to predictive values from the model) for (a) stress at break (b) strain at break (c) modulus and (d) crystallinity. The data points colored red, green, and blue corresponds to the results obtained at the highest, medium, and lowest temperature setting.

Regression model evaluation

To assess the relationship between the 3D printing process parameters (nozzle temperature, print speed, layer height, and wait-time) and the responses (flexural stress at break, strain at break, modulus, and crystallinity), a linear regression model was developed by fitting the data using a least square method (see Regression model evaluation section in ESI for details). To assess the accuracy of the model, responses from experimental measurements were plotted against the predicted values obtained from the linear regression model (*actual-by-predicted plot*) in Figure 5. If the model prediction is perfectly accurate, i.e., the prediction values are equal to the measured values, then all data points will fall on a diagonal line. The actual-by-predicted plots showed that the data points (black circular markers) are closely scattered around the diagonal line (solid red line). The blue horizontal line represents the mean of the measured responses, and the shaded red area around the diagonal line corresponds to the 95% confidence interval band for the mean effect. The shaded red area for all fitted models did not entirely overlap with the blue horizontal line, confirming that the model is significant in explaining the responses' variations. Furthermore, all models had a small p-value (a value

calculated from the overall analysis of variance (ANOVA report), a high Adjusted R-Square value (Rsq Adj), and a relatively small root mean square error (RSME) (Table S2, ESI). All of these indicate that the significant factors in the model were identified correctly and each model has a good predictive capability.

Table 4. Ranking of the influence of processing parameter on mechanical/thermal properties of the 3D printed PEEK specimens.

	T	PS	LH	WT
σ_f	++++	0	--	---
ε_f	++++	+++	0	0
E_f	0	0	----	0
$\chi(\%)$	++++	-	++	---

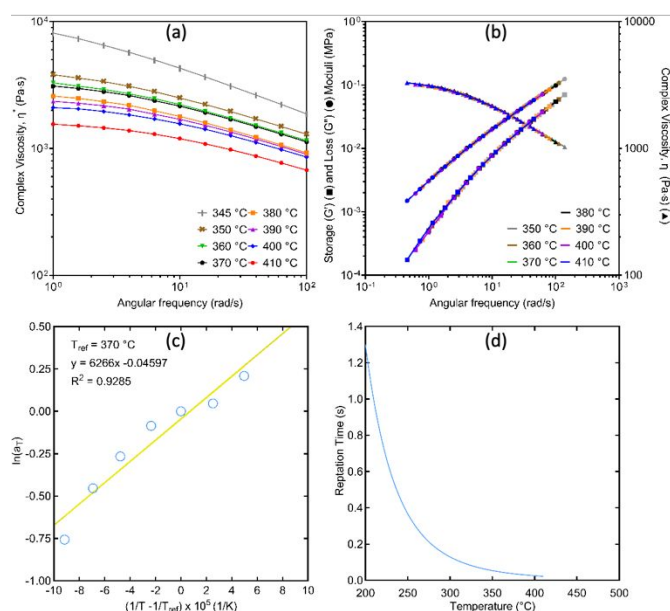


Figure 6. (a) Complex melt viscosity curves with respect to angular frequency measured at a temperature range from 345°C to 410°C. (b) Time-temperature-superposition (TTS) master curve showing storage modulus (G') and loss modulus (G'') values and complex viscosity (η^*). (c) Shift factor (a_T) values obtained from TTS plot fitted by an Arrhenius equation (Eq. 2). (d) Calculated reptation time (τ) curve with respect to temperature.

The rheological behaviour of PEEK

To investigate the PEEK melt flow properties and melt chain dynamics during printing process, offline rheological measurements were performed (Figure 6). It is known that a decrease in viscosity leads to an increase in surface wetting of the freshly printed layer on previously printed layer.⁴¹ The change in melt viscosity with respect to angular frequency (ω) for a range of temperature (345°C to 410°C) is given in Figure 6a. The viscosity curves shift down to lower viscosity ranges with increasing temperature, and for a constant temperature, the viscosity decreased with increasing ω . We also provided the zero-shear viscosity (η_0) values, obtained using the Williamson model, in Table S3 (ESI), which decreased with increasing

temperature. In addition to melt viscosity, the enhanced mobility of the polymer chains (reptation) during printing process could lead to chain diffusion and entanglement across the print interface.^{42, 43} The chain diffusion stops when the temperature at the interface drops below T_g , or it can be hindered by crystallization. Therefore, the time scale of the polymer chain mobility (i.e., the reptation time) is critical in determining the interlayer bond strength.^{44, 45} Here, we investigated the relationship between the reptation time (τ) and print temperature. Figure 6b shows the time-temperature-superposition (TTS) plot for PEEK at a reference temperature (T_{ref}) of 370°C. The TTS curve shows the change in storage (G') and loss modulus (G'') with respect to ω . The plot also shows the complex viscosity (η^*) as a function of ω . Our results showed that it was not possible to reach to a plateau modulus (G^0) or to observe a $G'-G''$ crossover, which is defined as G^0 for polydisperse polymers,⁴⁶ within our experimental capability. Therefore, we used the G^0 value for PEEK ($\sim 10^5$ Pa, obtained from $G'-G''$ crossover) reported by Rosa et al.⁴⁷ The reptation time can be approximated by Equation 1:⁴⁸⁻⁵¹

$$\tau(T) \approx \eta_0(T)/G^0 \quad (1)$$

The reptation time at the reference temperature, $\tau(T_{ref})$, was calculated to be 0.04 s. TTS curve allowed us to determine the shift factors (a_T) (Table S3, ESI). We then extrapolated the a_T for temperatures beyond our measuring capability by assuming an Arrhenius relationship between a_T and temperature (Figure 6c, with $R^2 = 0.964$):

$$a_T(T) = \exp\left[\frac{-\Delta H}{R}\left(\frac{1}{T} - \frac{1}{T_{ref}}\right)\right] \quad (2)$$

where R is the gas constant and ΔH is the activation enthalpy. This allowed us to determine the reptation time as a function of temperature, $\tau(T)$, by using Equation 2 (Figure 6d):

$$\tau(T) = \tau(T_{ref}) \times a_T(T) \quad (3)$$

which is plotted in Figure 6d. The τ decreased with increasing print temperature, such that τ was equal to 0.04 s, 0.03 s, and 0.02 s for $T = 370^\circ\text{C}$, 390°C , and 410°C , respectively. The shorter τ at higher print temperatures could lead to higher polymer chain mobility facilitating the diffusion and entanglement process across the interface between the freshly printed and the previous layer leading to a stronger interlayer bonding strength.

The effects of process parameters on flexural and thermal behaviour of the 3D printed PEEK samples

The strength and direction of the correlation between the factors and the responses are summarized in Table 4 (Figure S2, ESI). A plus (+) or a minus (-) sign is used to indicate a positive or a negative correlation with the response, respectively, while zero (0) represents an insignificant factor. The number of the (+) and (-) corresponds to the factor rankings in terms of

importance, such that 4 signs (+++, or ---) denote the most important factor whereas 1 sign (+, or -) represents the least important factor in the model. Our results showed that the flexural stress at break was strongly dependent on the nozzle temperature, and it increased with an increase in nozzle temperature. This can be due to (i) the increase in PEEK melt viscosity (Figure 6a) with nozzle (print) temperature, which could promote the wettability of the printed layer on the previously printed layer, and (ii) the decrease in τ , i.e., increase in chain mobility, with nozzle temperature (Figure 6d), which could facilitate the chain diffusion and entanglement across the interface between the printed layers, leading to a stronger interlayer bonding strength. Both the wait-time and the layer height have a negative effect on stress at break. The wait-time can determine the amount of cooling and the actual temperature of the top layer. Thus, a short wait-time could enhance the adhesion of the printed layer to the previously printed layer, whereas a long wait-time could lead to a significant temperature drop in the printed layer. When such a drop in temperature reaches below the crystallization temperature by the time the next layer is deposited, it could limit the intermolecular diffusion between the freshly printed and the previously printed layer. Moreover, the reduction in stress at break with respect to increasing layer height can be attributed to the presence of micro-sized voids between layers (Figure 7), resulting in a weaker interlayer bonding and stress at break. When the layer height is set small (below 0.2 mm), the layers can closely stack together. However, with larger layer heights, larger-sized voids between layers might form, resulting in weaker interlayer bonding and stress at break.

increase in stress, and can be due to the same reason, as better contact and more thermal fusion of the polymer chains across layers would occur at elevated nozzle temperatures. The surprising result is that the strain at break increased as the print speed increased. At higher print speeds, the amount of plastic extruded through the nozzle per unit time has to increase to ensure deposition of the same amount of material at lower speeds to print the exact same structure. Thus, the time required to melt the polymer at the nozzle is significantly reduced. On the other hand, when the object is printed faster, the struts within each layer have less time to cool down before the next strut is deposited, thus, leading to a better bonding and less void formation between struts (Figures 7b and 7c). Our results ruled out the latter outcome (or the positive effect) of print speed on the welding between layers. Some of the previously published works^{34,52} concluded that the sooner the subsequent layer was deposited (at higher print speeds), a significantly reduced time for the previously printed layer to cool down, resulting in stronger bonding between the printed layers. This explanation does not apply to our results since the effects of the print speed and the amount of cooling between layers were decoupled in this study by introducing the wait-time as an independent factor. In our case, we believe that the print speed is mainly influencing the intra-layer properties of the printed parts. Thus, we suggest that at higher print speeds, the adverse outcome of the shorter time of thermal exposure of the polymer at the nozzle and the positive effect of shorter cooling time between printing the adjacent struts cancel each other out, leading to a more uniform layer with fewer voids (confirmed with micro-CT images shown in Figure 7c). At lower print speeds, the polymers experienced prolonged time to melt at the nozzle, and the amount of cooling between printed struts varied mostly with the position of the printed strut. For instance, the struts at the corners experienced much less cooling than the straight segments (infill region, Figure 1a), causing uneven layer surfaces and more surface defects (Figure 7b). The stress can concentrate around these surface defects, which can result in a lower strain at break. Notice that the regression analysis suggested that the effect of speed was much more pronounced for the samples prepared at the highest nozzle temperature (410°C). This observation might suggest an interaction between the nozzle temperature and the print speed. Although the interaction cannot be fully resolved from a resolution IV design developed in this study, we plan to investigate the interactions between factors in the future study.

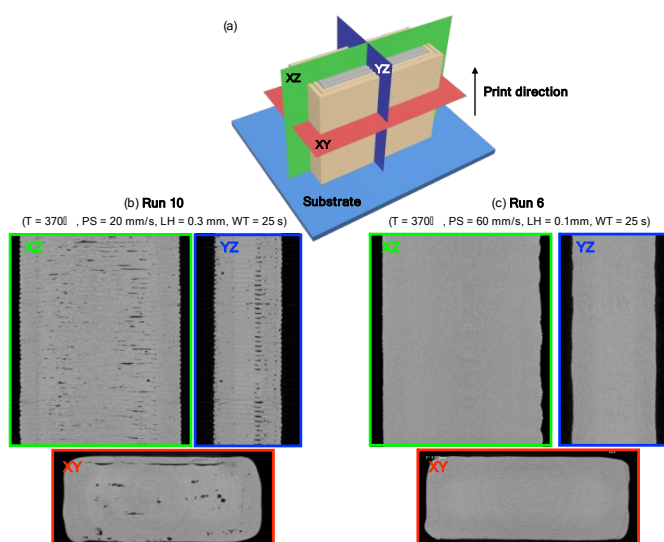


Figure 7. (a) 3D view of the reconstructed samples in XZ (coronal, green), YZ (sagittal, blue), and XY (transaxial, red) planes to visualize the internal defects. (b) Representative micro-CT image of a test sample from Run 10. Voids can be found between layers and between infill strands (overall porosity: 2.3%). (c) Representative micro-CT image of a test sample from Run 6. More uniform layers with fewer voids comparing to samples printed at lower speed and larger layer height (overall porosity: 0.07%).

Our results showed that the strain at break increased with increasing temperature, which is expected considering the

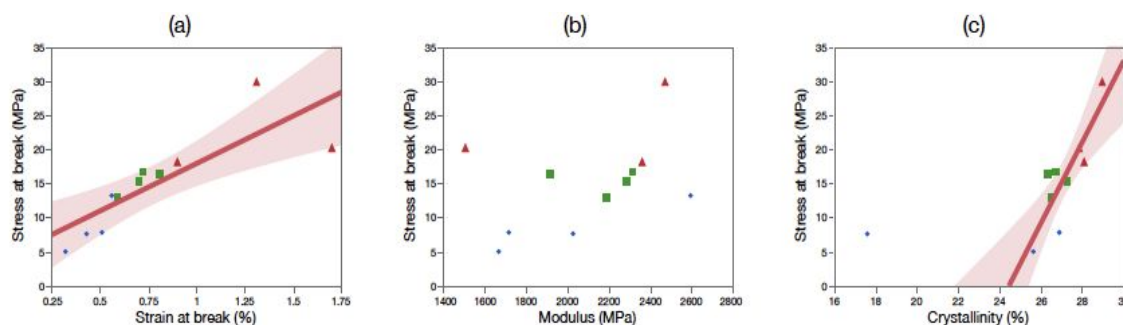


Figure 8. Stress at break plotted against (a) strain at break, (b) modulus and (c) crystallinity. The blue circles, green squares and red triangles represent the data obtained from samples printed at the lowest (370°C), medium (390°C) and highest temperatures (410°C), respectively. Positive correlations were observed for stress vs. strain and stress vs. crystallinity. However, there is no significant trend in modulus with respect to stress at break. The shaded band is the 95% confidence interval of the fitted line.

When the flexural modulus is considered, layer height was found to be the only significant factor, such that the modulus decreased with increasing layer height. This relationship can be explained considering the same reason for the decrease in stress at break with increasing layer height, such that more voids are generated at higher layer thicknesses. Moreover, this observation can also be explained by considering the fact that the layer thickness is inversely proportional to the number of printed layers. In the experimental setup, the tensile stress was normal to the individual layers, which carried and transferred most of the applied load. With a decrease in the layer height, more layers needed to be printed (to complete the same size/volume of the sample), splitting the applied load by the layers and leading to an increase in the modulus. It is interesting to note that the layer height was found to be the only factor that exerts the influence on modulus. The most influential temperature-related parameters, such as nozzle temperature and wait-time, which significantly affect thermal fusion between layers, are not relevant here. This indicates that the interlayer bonding strength has a negligible effect and weak correlation with the modulus.

For crystallinity of the PEEK post-printing, the nozzle temperature has the most substantial positive effect, followed by the wait-time with a strong negative effect, and the layer height with a moderate positive effect. The print speed has the lowest negative contribution to crystallinity. Previous studies have shown that the degree of crystallinity of semi-crystalline polymers highly depends on the cooling rate.^{53, 54} The nozzle temperature, wait-time, layer height, and print speed all have a direct or indirect impact on the cooling rate, and sequentially affect the crystallinity of the printed parts. The cooling rate is a result of the competition between the rate of heat loss from the printed struts and the rate of heat input from the nozzle. It is reasonable to state that a higher nozzle temperature would allow complete melting of the crystals and more prolonged exposure at elevated temperatures for the filaments, which can effectively increase chain mobility, facilitating the organization of polymer chains into crystal structures. When wait-time is considered, increasing WT leads to delayed printing, which can allow for cooling of the freshly printed layer prior to printing of

the following layer. Therefore, the previously printed layer may not be exposed to elevated temperatures long enough for polymer chains to rearrange themselves and form crystalline structures. Layer thickness also has a thermal effect on the printed parts. On the one hand, a thicker layer height can provide more extruded material and retains heat for a longer period of time (slower heat loss), favoring the formation of a crystalline structure. On the other hand, as the layer height increases, the heat generated by the freshly printed layer needs to penetrate (within a previously printed layer) a thicker layer height, potentially reducing the reheating depth of the previously deposited layer, and resulting in a lower crystallinity. Our results showed that the former effect was more dominant in our case. Finally, the print speed showed the least effect on crystallinity, where an increase in the print speed led to a decrease in crystallinity. As discussed above, a rapid print speed shortens the heat exposure time at the nozzle and increases the cooling rate. The rapid cooling allows less time for crystallization to occur. In agreement with our observations, Rinaldi et al. suggested that the shorter thermal exposure could result in the presence of small crystals in the partially molten polymers, which acts as seeds to initiate cold crystallization.³ This was observed for *Run 6* (Figure 4b), which was printed at the lowest temperature (370°C), longest wait-time (25s), smallest layer height (0.1 mm), and the fastest print speed (60 mm/s) in this study. Note that it has been found that a higher degree of crystallization can be achieved in some FFF-printed semi-crystalline polymers such as PCL⁵⁵ and PLA⁵⁶ due to the effect induced by the high shear flow during printing, which can increase the number of nucleation sites for crystals and accelerate crystallization speed. As a result, flow-induced crystallization (FIC) could occur for lower print temperatures and faster shear rates (i.e., print speeds).⁵⁷ However, our experimental data did not demonstrate an increase in the degree of crystallization with print speed. The discrepancy could arise from the stiffer character of the PEEK chains,⁵⁸ making them hard to align with the shear direction. The discrepancy could also be attributed to the prepared sample geometry. In contrast to literature,^{55, 56} where a single filament or a single wall comprised of multiple filaments were considered, in this work, a thick and large-scale component with multiple tool

paths could result in more extensive heat retention and thus a slower cooling profile, allowing stretch relaxation of the polymer chains prior to the onset of crystallization. Consequently, FIC has little effect on the degree of crystallization. Additional structure and thermal characterization at the welding zone can be performed using in-situ wide-angle X-ray scattering and infrared spectroscopy⁵⁹ and is the subject of future work.

Overall, our results suggest that the nozzle temperature is the most critical parameter, which has a strong positive effect on stress at break, strain at break, and crystallinity, but has a negligible effect on modulus. The second most important parameter is the layer height, with an adverse effect on stress at break and modulus, but a higher setting is preferential for enhanced crystallinity. Wait-time ranks as the third influential parameter, and a lower wait-time is favored for higher stress at break and crystallinity. The effect of wait-time on the interlayer bonding strength has only been discussed in a few papers.^{19, 60, 61} The wait-time is determined by the print speed, the dimensions of the printed samples, the strand deposition path, and the number of simultaneously printed specimens. Therefore, the wait-time should be considered as an important (and an independent) factor affecting the interlayer bonding strength of the 3D printed parts. Finally, the least important parameter was found to be the print speed.

Correlations between properties of 3D printed samples

Here, we investigated the relationship between the responses (mechanical behavior and crystallinity). The level of stress/strain at break is a direct consequence of the interlayer bonding strength, and a positive trend was found between stress at break and strain at break for the experimental Runs (Figure 8a and Figure S4a, ESI), except for Run 3. Run 3 was excluded from the analysis due to print quality issues. No significant trend in modulus was observed with respect to stress at break (Figure 8b and Figure S4b, ESI), indicating that the modulus was not closely related to interlayer bonding strength but dependent on the layer height (geometrical parameter) of the printed parts. It has been observed in some studies that an increase in crystallinity in the 3D printed specimens would greatly reduce ductility, causing delamination occurred at a much smaller strain.⁵⁹ However, we observed a positive relationship between crystallinity and stress/strain at break. (Figure 8c and Figure S4c, ESI). The positive correlation found between crystallinity and stress at break might also be attributed to the fact that the same factors influenced both the stress at break and crystallinity. The parts printed with higher temperatures have larger heat retention and slower cooling rate, which can delay the time of onset of crystallization, and thus promotes polymer chain interdiffusion across the interface. The polymer chains maintain at higher temperatures for a longer period of time can also lead to a significantly higher degree of crystallization. Therefore, a positive relationship between stress/strain at break and crystallinity was observed. We also found a positive correlation between strain at break

and crystallinity, but no correlation was found between strain at break and modulus, and modulus and crystallinity (Figure S5, ESI). The red regression lines in Figure 8 show the relationship between stress at break and strain at break (Stress at break = $4.02 + 13.93 \times$ Strain at break, $p = 0.0021$) and stress at break and crystallinity (Stress at break = $-145.54 + 5.95 \times$ Crystallinity, $p = 0.0016$). For instance, the stress at break increased by around 14 MPa and 6 MPa for every unit increase in strain at break and crystallinity, respectively. Note that the regression line fits well for most of the data in Figure 8c except for Run 6. One possible explanation is that the stress at break reached its lower limit for Run 6 and became independent of crystallinity. Further study is needed to confirm the correlation among these two parameters at the lower end of crystallinity.

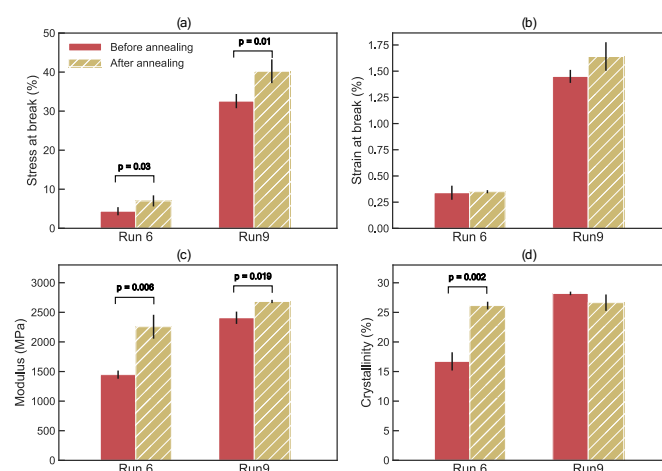


Figure 9. Influence of heat treatment on the mechanical performance and crystallinity of Run 6 and Run 9 samples: (a) stress at break, (b) strain at break, (c) modulus, and (d) crystallinity.



Figure 10. Pictures of the annealed test samples. (a) Run 6 ($T = 370^{\circ}\text{C}$, $\text{PS} = 60 \text{ mm/s}$, $\text{LH} = 0.1 \text{ mm}$, $\text{WT} = 25 \text{ s}$) and (b) Run 9 ($T = 410^{\circ}\text{C}$, $\text{PS} = 60 \text{ mm/s}$, $\text{LH} = 0.1 \text{ mm}$, $\text{WT} = 11 \text{ s}$) samples after thermal annealing. Run 6 sample was found to be deformed while Run 9 sample remained flat after thermal treatment.

Effect of thermal annealing

To investigate the role of thermal annealing on layer bonding strength and the degree of crystallinity, 3D-printed samples with the lowest crystallinity (Run 6, $T = 370^{\circ}\text{C}$, $\text{PS} = 60 \text{ mm/s}$, $\text{LH} = 0.1 \text{ mm}$, $\text{WT} = 25 \text{ s}$) and the (second) highest crystallinity (Run 9, $T = 410^{\circ}\text{C}$, $\text{PS} = 60 \text{ mm/s}$, $\text{LH} = 0.1 \text{ mm}$, $\text{WT} = 11 \text{ s}$) were chosen. The stress/strain at break, modulus, and crystallinity of Run 6 and Run 9 samples before and after annealing are shown in Figure 9. The stress at break and modulus showed a significant increase after annealing for both Runs. The value of stress at break for Run 6 and Run 9 are equal to $4.4 \pm 1 \text{ MPa}$ and $32.6 \pm 1.8 \text{ MPa}$, respectively. After annealing, these values increased to $7 \pm 1.4 \text{ MPa}$ (~60% increase) and $40.2 \pm 3 \text{ MPa}$ (~25% increase) for Run 6 and Run 9, respectively. For Run 6, the modulus significantly increased from $1447.4 \pm 68.8 \text{ MPa}$ to

2256.9 ± 201.4 MPa after annealing, while the modulus increased slightly from 2408.2 ± 103.7 MPa to 2683.2 ± 27 for Run 9. The strain at break did not change significantly with thermal annealing. The degree of crystallinity for Run 6 increased greatly after annealing, from 16.7 ± 1.5% to 26.2 ± 0.7%. For Run 9, the degree of crystallinity remained approximately the same after annealing (~27%). We believe that Run 9 sample already reached its maximum achievable crystallinity for PEEK post-printing, and thus, eliminating the effect of annealing on crystallinity. The observed increase in mechanical properties, including stress at break and modulus in PEEK samples, can be attributed to the complex interplay of multiple factors, including residual stress, diffusion of polymer chains across the interface, the presence of the internal voids, and the degree of crystallinity. Typically, thermal annealing leads to a reduction in residual stresses (developed during the printing process) as well as higher mobility of the polymer chains, and thus, enhances the welding at the interface, which can explain the increase in mechanical properties of the Run 9 samples. The presence of internal voids has been shown to have an adverse impact on mechanical properties. We found that the porosity in Run 6 sample increased significantly from 0.097% to 0.36%, whereas the porosity in Run 9 sample was approximately the same after annealing (within the range of 0.53% - 0.48%). This observation could be explained as follow: lower print temperatures and longer wait-times (such as for Run 6) resulted in higher residual stresses post-printing as compared to higher print temperatures and shorter wait-times (such as for Run 9). The residual stress has been shown to be relieved through deformation during thermal treatment⁶², i.e., the reduction in residual stress was usually accompanied with structural deformation. Because more residual stress was built up in Run 6 during the printing process, a greater amount of residual stress was relieved during thermal annealing, leading to a larger deformation, as can be seen in **Figure 10**. Thus, annealed Run 6 sample was more prone to void formation. In contrast, there was no noticeable deformation in annealed Run 9 sample, and thus, the porosity remained the same. The overall increase in stress at break and modulus for Run 6 samples suggested that the contribution to increased polymer chain mobility at the interface and the reduced residual stress during annealing are the two dominant factors as compared to the porosity. In addition, it is worth mentioning that although an increase in stress at break was found in Run 6 samples after annealing, the value of the stress at break was still much lower when compared to that of Run 9 sample, indicating that the interlayer bonding strength was mainly determined during the printing process. The thermal treatment after printing can only slightly improve the bonding strength. In contrast, thermal treatment can significantly improve the modulus and crystallinity. For instance, the annealed Run 6 samples showed significantly enhanced modulus and crystallinity, reaching that of the Run 9 samples. Some researchers have suggested that increasing crystallinity might slow down the diffusion of polymer chains across the interface during annealing.^{63, 64}

Conclusions

This is the first study, to our knowledge, to systematically investigate the relationship between interlayer bonding strength of 3D printed PEEK and process parameters. The interlayer bonding strength of the FFF-printed PEEK samples was evaluated by a three-point flexural test. The samples were printed vertically, and a bending load was applied perpendicular to the layers, such that the load was carried across layers. A DOE approach was developed to study the influence of the process parameters (including nozzle temperature, print speed, layer height, and wait-time) on the mechanical properties (flexural stress/strain at break, flexural modulus) and crystallinity of the printed parts. Different from previous studies, the effect of print speed and the amount of cooling between layers were decoupled by introducing the wait-time as an independent factor. The following conclusions have been drawn from this study:

1. The most important parameters determining flexural stress at break are nozzle temperature, followed by wait-time and layer height. A higher nozzle temperature, a shorter wait-time, and a smaller layer height led to greater stress at break. For strain at break, higher nozzle temperature and print speed were preferable. Layer height was found to be the only significant factor to control the modulus, such that an increase in layer height negatively affected the modulus. All four process parameters were found to have an impact on crystallinity, and it was demonstrated that a higher crystallinity could be obtained by increasing the nozzle temperature, decreasing the wait-time, increasing the layer height, and decreasing the print speed.
2. The observed dependence of material's properties on the process parameters suggested that the nozzle temperature is the most influential factor, followed by the layer height and wait-time, while print speed played a minor role.
3. We found a strong correlation between flexural stress at break and strain at break, while no significant correlation was found between flexural stress/strain at break and modulus. An implication of this result is that the flexural stress/strain at break is an adequate indicator of the material's interlayer bonding strength, and the flexural modulus is more of a geometric property that is mainly determined by the layer height.
4. Finally, we demonstrated that annealing (thermal treatment) could effectively increase the stress at break, modulus, and crystallinity of the samples post-printing. However, the enhanced values of stress at break, and thus interlayer bonding strength, of the weak samples were still much lower than that of the best-performing sample groups.

Up until now, there has been no standard existed for testing the mechanical properties of the 3D-printed PEEK materials, especially their interlayer bonding strength. We strongly believe

that the approach presented in this study and findings provide an important step towards the establishment of a framework for developing standardized tests for understanding the interlayer behavior of the FFF-printed PEEK samples.

Experimental

Design of Experiment (DOE) model

In the interest of saving time and money, we developed a *screening design*, or so-called *fractional factorial design (FFD)*. In this study, four independent *factors* (i.e., processing parameters), including nozzle temperature (T), print speed (PS), print layer height (LH), and wait-time between print layers (WT) (Table 2), were investigated. The wait-time refers to the amount of time each layer was allowed to cool before the sequential layer is deposited. The levels of factors, i.e., the high (+) and low (-) setting for each processing parameter, were selected based on the recommended print settings for PEEK filaments and the preliminary tests performed in our laboratory. The design also included four center points (denoted as 0000) to assess reproducibility. The JMP Pro 14 software was used to generate the experimental design matrix (Table 3). The measurements, denoted as responses, include flexural stress at break, strain at break, modulus, and crystallinity.

3D printing of test samples

Funmat HT printer (Intamsys, Shanghai, China) was used to fabricate the test samples. Digital 3D models were designed and developed in Fusion 360. Flexural test samples were designed based on ISO 178 standard (10 mm × 4 mm × 80 mm). The model files were imported into Instamsuite (Intamsys slicing software) to set the printing parameters, which were determined by DOE model (Table 2). In order to improve the print quality and prevent layer delamination, the print chamber temperature was set to 80°C, and equilibrated for (at least) 45 min prior to printing. No additional heating was applied to the substrate. To enhance the attachment of the first layer to the print substrate, a PEI (poly(etherimide)) sheet was attached to the build platform prior to printing. The first two layers were printed at a lower speed (20 mm/s) to ensure good substrate adhesion. PEEK filaments (Essentium, Texas, USA) with 1.75 mm in diameter were fed into a 0.4 mm diameter nozzle. The flexural specimens, shown in Figure 1, were fabricated in the vertical orientation (with the largest dimension, 80mm, in the z-axis). Two shell layers were printed with 100% infill setting and a linear infill pattern parallel to the longer side of the contour. During printing, a retraction length of 4.5 mm and a retraction speed of 45 mm/s were used to prevent stringing and oozing of the filament. To vary the wait-time, i.e., the delay time between printing of subsequent layers, two to nine test samples were printed simultaneously. The number of simultaneously printed samples determined the wait-time for a specific print speed (spacing between specimens was kept constant). For example, it takes ~2.78s to print one layer for one specimen when using a print speed of 60 mm/s. Therefore, 9 samples were required to print to achieve a wait-time of 25s (2.78*9) and 4 samples to

achieve a wait-time of 11s (2.78*4). For a print speed of 40 mm/s, it takes 3.6s to print one layer for one specimen, and therefore 5 samples were printed (3.6*5) to ensure that the wait-time is 18s. For a print speed of 20 mm/s, it takes ~6.2s to print one layer for one specimen. We printed 2 samples (6.2*2) to approximate the wait-time of 11s and 4 samples to achieve a wait-time of 25s (6.2*4). Simultaneous printing of multiple samples is preferred to control the wait-time rather than keeping the nozzle idle (by stopping extrusion) due to a significant amount of material oozing from the nozzle when the nozzle was idle. Note that this a common practice to fabricate hard-to-print samples in industry settings. Large-scale manufacturing that requires 3D printing multitude of samples on the same print substrate also leads to delays between print layers during printing. After completing the print job, the chamber heater was turned off, and the samples were kept in the chamber for 1 hour to prevent a sudden drop in temperature, which could lead to layer delamination in the printed samples. All specimens were tested without further thermal treatment unless otherwise specified.

To study the influence of annealing on interlayer bonding strength and crystallinity, the specimens were thermally treated post-printing. For this purpose, samples were first dried at 150°C for one hour in a Heratherm™ Advanced Protocol oven (Thermo Scientific™), followed by ramping up the temperature to 200°C (3°C/min) and samples were kept at this temperature for two hours. The samples were then cooled to 150°C (1.5°C/min) and held for 30 minutes. The oven temperature was set to 60°C allowing the samples to cool down below the glass transition temperature of the PEEK.

Three-point flexural testing

Three-point flexural tests were carried out on an Instron 2712 universal testing machine (Instron Co., Ltd, MA, USA) with a 1 kN load capacity. During the flexural tests, the test sample lay horizontally on two metal support rods (5 mm in radius and 40 mm apart from each other). A preload of 0.5-1.5 N at 0.05 mm/min was applied to ensure good contact between the compression plate and the sample. After the contact was established, a compression force was applied at a rate of 1 mm/min to the top of the sample through a support rod of the same size, which was placed halfway of the support span. The test was completed when the specimen broke or when the specimen reached 3.5% deflection. Load (P) and crosshead displacement (δ , or beam deflection) were recorded. P and δ were converted to flexural stress (σ_f) and flexural strain (ϵ_f) using the following equations:

$$\sigma_f = \frac{3PL}{2bd^2} ; \quad \epsilon_f = \frac{6\delta d}{L^2} \quad (4)$$

where L is the length of support span, b is the width, and d is the thickness of the test beam. δ is the deflection of the center of the beam at a given moment. The flexural modulus (E_f) was calculated using the following equation:

$$E_f = \frac{L^3 m}{4bd^3} \quad (5)$$

In this equation, m is the slope of the straight-line portion of the load-deflection curve. Flexural properties including stress at break, strain at break, and modulus, were calculated. At least three replicates were tested for each sample group (or *Run*).

Thermal measurements

Thermal profiles of the printed PEEK specimens were examined using a differential scanning calorimeter (DSC, 6000 DSC from Perkin Elmer, Inc., MA, USA). The samples for DSC measurement were cut from the center of a single layer from the printed specimen. We did not notice any significant difference in the degree of crystallinity from the center and the outer shell region for all runs except for *Run* 6. For *Run* 6, a lower degree of crystallization was found in the outer shell region. Samples (~7-9 mg) were placed in an aluminum pan and heated from 30°C to 400°C at a rate of 10°C/min under nitrogen gas. The first heating scan was recorded to investigate the effect of the printing process on the thermal history of the printed test samples. The crystallinity of the PEEK was determined by the following equation:

$$\chi(\%) = \frac{\Delta H_{endo} + \Delta H_{exo}}{130} \times 100\% \quad (6)$$

where ΔH_{endo} (J/g) and ΔH_{exo} (J/g) are the enthalpy obtained by integrating the area under the melting peak and the cold-crystallization peak, respectively, and 130 (J/g) is the heat of fusion of a 100% crystalline PEEK.⁶⁵

Morphological observations

Micro-computed tomography (micro-CT) was used to image the samples to investigate the internal void content (porosity), void distribution, and morphology. A Skyscan 1275 μ -CT scanner (Bruker Corp., Billerica, MA, USA) was used, which uses an X-ray source of 10 W, a voltage of 43 kV, and a current of 200 mA. The scanning was obtained using a rotation step of 0.2° (360° scan) and exposure time of 42 ms, at an image pixel size of 12 μ m, with an image size equal to 1536 \times 1944 pixels. After the image acquisition step, the images were reconstructed in NRecon (Bruker). The reconstructed images were saved in the coronal (XZ), sagittal (YZ) and transaxial (XY) planes using the Data View program (Bruker). The images were then analyzed using CTAn software (Bruker) to evaluate the total porosity, which includes the closed pores (empty spaces embedded in the material) and open pores (empty spaces in contact with air). After flexural tests, the fracture surface of the 3D printed specimens (coated with gold-platinum) was examined by a JSM-7900F field-emission scanning electron microscope (SEM) (JEOL USA, Inc.) at an accelerating voltage of 5kV. The average cavity diameter for each sample was determined at 10 different locations on 3 different SEM images using Fiji/ImageJ software.

Rheological measurements

Rheology was performed using a Discovery Hybrid Rheometer (DHR-2; TA Instruments, New Castle, DE, USA) fitted with a

parallel plate fixture at a gap distance of 500 μ m. A 1 N axial control was used to control gap distance. Additionally, an environmental test chamber was used to control temperature and to apply a steady flow of nitrogen at 10 l/min. The top plate was 25 mm in diameter and the bottom plate was 25 mm in diameter with a lip to allow the excess polymer to be trimmed before testing. The filament was cut into short fibers and placed on the plates at the desired temperature. Temperature equilibration was achieved before all tests began. Frequency sweeps and flow ramps were performed from 1-100 rad/s and 0.1-100 s⁻¹, respectively (at 345°C, and 350°C - 410°C at 10°C intervals). All tests were performed within a 180s time span to mitigate the effects of polymer degradation.

Conflicts of interest

There are no conflicts to declare.

Acknowledgements

This study is partially funded by the National Science Foundation Award Number DMR-1714882 and the New Jersey Institute of Technology Faculty Start-up Funds. The authors would like to thank Prof. David Venerus for his suggestions for rheological studies, Dr. Mirko Schoenitz for his helpful advice on mechanical testing, and Andrew House for the preparation of samples.

References

1. M. Dawoud, I. Taha and S. J. Ebeid, *Journal of Manufacturing Processes*, 2016, **21**, 39-45.
2. D. Odell, P. K. Wright, M. Montero, S. Roundy and S. H. Ahn, *Rapid Prototyping Journal*, 2002, **8**, 248-257.
3. M. Rinaldi, T. Ghidini, F. Cecchini, A. Brandao and F. Nanni, *Composites Part B: Engineering*, 2018, **145**, 162-172.
4. R. J. Zaldivar, D. B. Witkin, T. McLouth, D. N. Patel, K. Schmitt and J. P. Nokes, *Additive Manufacturing*, 2017, **13**, 71-80.
5. J. R. C. Dizon, A. H. Espera, Q. Chen and R. C. Advincula, *Additive Manufacturing*, 2018, **20**, 44-67.
6. A. K. Ravi, A. Deshpande and K. H. Hsu, *Journal of Manufacturing Processes*, 2016, **24**, 179-185.
7. M. Mabrouk, G. T. El-Bassouini, H. H. Beherei, S. H. Kenawy and E. M. A. Hamzawy, in *Advanced 3D-Printed Systems and Nanosystems for Drug Delivery and Tissue Engineering*, eds. L. C. d. Toit, P. Kumar, Y. E. Choonara and V. Pillay, Elsevier, 2020, DOI: <https://doi.org/10.1016/B978-0-12-818471-4.00004-2>, pp. 83-107.
8. A. Marzola, E. Mussi and F. Uccheddu, Cham, 2020.
9. A. Das, C. A. Chatham, J. J. Fallon, C. E. Zawaski, E. L. Gilmer, C. B. Williams and M. J. Bortner, *Additive Manufacturing*, 2020, **34**, 101218.
10. S. Singh, C. Prakash and S. Ramakrishna, *European Polymer Journal*, 2019, **114**, 234-248.
11. M. C. Sobieraj and C. M. Rimnac, in *PEEK Biomaterials Handbook*, ed. S. M. Kurtz, William Andrew Publishing, Oxford, 2012, DOI: <https://doi.org/10.1016/B978-1-4377-4463-7.10005-3>, pp. 61-73.

12. P. Wang, B. Zou, H. Xiao, S. Ding and C. Huang, *Journal of Materials Processing Technology*, 2019, **271**, 62-74.
13. B. Valentan, Z. Kadivnik, T. Brajlilh, A. Anderson and D. Igor, *Materiali in Tehnologije*, 2013, **47**, 715-721.
14. C. Yang, X. Tian, D. Li, Y. Cao, F. Zhao and C. Shi, *Journal of Materials Processing Technology*, 2017, **248**, 1-7.
15. W. Z. Wu, P. Geng, J. Zhao, Y. Zhang, D. W. Rosen and H. B. Zhang, *Materials Research Innovations*, 2014, **18**, S5-12-S15-16.
16. F. Zhao, D. Li and Z. Jin, *Materials*, 2018, **11**.
17. M. Vaezi and S. Yang, *Virtual and Physical Prototyping*, 2015, **10**, 123-135.
18. R. Wang, K.-j. Cheng, R. C. Advincula and Q. Chen, *MRS Communications*, 2019, **9**, 1046-1052.
19. M. F. Arif, S. Kumar, K. M. Varadarajan and W. J. Cantwell, *Materials & Design*, 2018, **146**, 249-259.
20. X. Deng, Z. Zeng, B. Peng, S. Yan and W. Ke, *Materials*, 2018, **11**.
21. P. Geng, J. Zhao, W. Wu, W. Ye, Y. Wang, S. Wang and S. Zhang, *Journal of Manufacturing Processes*, 2019, **37**, 266-273.
22. Q. Li, W. Zhao, Y. Li, W. Yang and G. Wang, *Polymers*, 2019, **11**.
23. M. Luo, X. Tian, J. Shang, W. Zhu, D. Li and Y. Qin, *Composites Part A: Applied Science and Manufacturing*, 2019, **121**, 130-138.
24. A. El Magri, K. El Mabrouk, S. Vaudreuil, H. Chibane and M. E. Touhami, *Journal of Applied Polymer Science*, 2020, **n/a**, 49087.
25. D. Garcia-Gonzalez, A. Rusinek, T. Jankowiak and A. Arias, *Composite Structures*, 2015, **124**, 88-99.
26. K. M. Rahman, T. Letcher and R. Reese, 2015.
27. X. Han, D. Yang, C. Yang, S. Spintzyk, L. Scheideler, P. Li, D. Li, J. Geis-Gerstorfer and F. Rupp, *J Clin Med*, 2019, **8**, 240.
28. W. Wu, P. Geng, G. Li, D. Zhao, H. Zhang and J. Zhao, *Materials (Basel)*, 2015, **8**, 5834-5846.
29. P. Han, A. Tofangchi, S. Zhang, A. Desphande and K. Hsu, *Procedia Manufacturing*, 2020, **48**, 737-742.
30. M. Luo, X. Tian, W. Zhu and D. Li, *Journal of Materials Research*, 2018, **33**, 1632-1641.
31. S. Berretta, R. Davies, Y. T. Shyng, Y. Wang and O. Ghita, *Polymer Testing*, 2017, **63**, 251-262.
32. P. Consul, A. Chaplin, N. Tagscherer, S. Zaremba and K. Drechsler, *Polymer International*, 2020, **n/a**.
33. C. Basgul, T. Yu, D. W. MacDonald, R. Siskey, M. Marcolongo and S. M. Kurtz, *Journal of the Mechanical Behavior of Biomedical Materials*, 2020, **102**, 103455.
34. J. Coogan Timothy, *Rapid Prototyping Journal*, 2017, **23**, 414-422.
35. C. S. Davis, K. E. Hillgartner, S. H. Han and J. E. Seppala, *Additive Manufacturing*, 2017, **16**, 162-166.
36. J. E. Seppala, S. Hoon Han, K. E. Hillgartner, C. S. Davis and K. B. Migler, *Soft Matter*, 2017, **13**, 6761-6769.
37. R. Morrell, *NPL Measurement Good Practice Guide*, 1997, **No. 7**.
38. S. Wang, Y. Zhang and G. Wu, *Materials (Basel)*, 2018, **11**, 1874.
39. V. E. Kuznetsov, A. N. Solonin, O. D. Urzhumtsev, R. Schilling and A. G. Tavitov, *Polymers*, 2018, **10**, 313.
40. K. R. Hart and E. D. Wetzels, *Engineering Fracture Mechanics*, 2017, **177**, 1-13.
41. X. Gao, S. Qi, X. Kuang, Y. Su, J. Li and D. Wang, *Additive Manufacturing*, 2021, **37**, 101658.
42. C. McIlroy and P. D. Olmsted, *Polymer*, 2017, **123**, 376-391.
43. T. Ge, F. Pierce, D. Perahia, G. S. Grest and M. O. Robbins, *Physical Review Letters*, 2013, **110**, 098301.
44. O. A. Ezekoye, C. D. Lowman, M. T. Fahey and A. G. Hulme-Lowe, *Polymer Engineering & Science*, 1998, **38**, 976-991.
45. J. Bartolai, W. Simpson Timothy and R. Xie, *Rapid Prototyping Journal*, 2018, **24**, 321-332.
46. M. Rubinstein and R. H. Colby, *Polymer physics*, Oxford university press New York, 2003.
47. M. Rosa, L. Grassia, A. D'Amore, C. Carotenuto and M. Minale, *AIP Conference Proceedings*, 2016, **1736**, 020177.
48. T. J. Coogan and D. O. Kazmer, *Additive Manufacturing*, 2020, **35**, 101368.
49. E. van Ruymbeke, C.-Y. Liu and C. Bailly, *Rheology Reviews*, 2007.
50. W. W. Graessley, in *The entanglement concept in polymer rheology*, Springer, 1974, pp. 1-179.
51. J. D. Ferry, *Viscoelastic properties of polymers*, John Wiley & Sons, 1980.
52. A. Q. Pan, Z. F. Huang, R. J. Guo and J. Liu, *Key Engineering Materials*, 2016, **667**, 181-186.
53. S. M. Kurtz and J. N. Devine, *Biomaterials*, 2007, **28**, 4845-4869.
54. S.-L. Gao and J.-K. Kim, *Composites Part A: Applied Science and Manufacturing*, 2000, **31**, 517-530.
55. C. McIlroy and R. S. Graham, *Additive Manufacturing*, 2018, **24**, 323-340.
56. C. McIlroy, J. E. Seppala and A. P. Kotula, in *Polymer-Based Additive Manufacturing: Recent Developments*, American Chemical Society, 2019, vol. 1315, ch. 6, pp. 85-113.
57. B. Nazari, A. M. Rhoades, R. P. Schaake and R. H. Colby, *ACS Macro Letters*, 2016, **5**, 849-853.
58. C. Fournies, M. Dosière, M. H. J. Koch and J. Roovers, *Macromolecules*, 1998, **31**, 6266-6274.
59. Y. Shmueli, J. Jiang, Y. Zhou, Y. Xue, C.-C. Chang, G. Yuan, S. K. Satija, S. Lee, C.-Y. Nam, T. Kim, G. Marom, D. Gersappe and M. H. Rafailovich, *ACS Applied Polymer Materials*, 2019, **1**, 1559-1567.
60. N. G. Morales, T. J. Fleck and J. F. Rhoads, *Additive Manufacturing*, 2018, **24**, 243-248.
61. E. Kuznetsov Vladimir, *Rapid Prototyping Journal*, 2019, **ahead-of-print**.
62. A. D'Amico Anthony, *Rapid Prototyping Journal*, 2017, **23**, 943-953.
63. S. Bhandari, R. A. Lopez-Anido and D. J. Gardner, *Additive Manufacturing*, 2019, **30**, 100922.
64. Y. M. Boiko, G. Guérin, V. A. Marikhin and R. E. Prud'homme, *Polymer*, 2001, **42**, 8695-8702.
65. D. J. Blundell and B. N. Osborn, *Polymer*, 1983, **24**, 953-958.